Bridging scales in a multiscale pattern-forming system

Laeschkir Würthner[1,*], Fridtjof Brauns[1,2,*], Grzegorz Pawlik[3], Jacob Halatek[1,4], Jacob Kerssemakers[3], Cees Dekker[3,†], and Erwin Frey[1,5,†]

[1]Arnold Sommerfeld Center for Theoretical Physics and Center for NanoScience, Department of Physics, Ludwig-Maximilians-Universität München, Theresienstraße 37, D-80333 München, Germany

[2]Present address: Kavli Institute for Theoretical Physics, University of California Santa Barbara, Santa Barbara, CA 93106, USA

[3]Department of Bionanoscience, Kavli Institute of Nanoscience Delft, Delft University of Technology, Van der Maasweg 9, 2629 HZ Delft, the Netherlands

[4]Research Department, Oxford BioMedica Ltd., Windrush Court, Transport Way, Oxford, OX4 6LT, UK

[5]Max Planck School Matter to Life, Hofgartenstraße 8, D-80539 Munich, Germany

[*]L.W. and F.B. contributed equally to this work.
[†]Corresponding authors. Email: frey@lmu.de or c.dekker@tudelft.nl

Abstract

Self-organized pattern formation is vital for many biological processes. Mathematical modeling using reaction-diffusion models has advanced our understanding of how biological systems develop spatial structures, starting from homogeneity. However, biological processes inherently involve multiple spatial and temporal scales and transition from one pattern to another over time, rather than progressing from homogeneity to a pattern. One possibility to deal with multiscale systems is to use coarse-graining methods that allow the dynamics to be reduced to the relevant degrees of freedom at large scales. Unfortunately, these approaches have the major disadvantage that the eliminated scales cannot be reconstructed from the large-scale dynamics and thus one loses the information about the patterns. Here, we present an approach for mass-conserving reaction-diffusion systems that overcomes this issue and allows one to reconstruct information about patterns from the large-scale dynamics. We illustrate our approach by studying the Min protein system, a paradigmatic model for protein pattern formation. By performing simulations, we first show that the Min system produces multiscale patterns in a spatially heterogeneous geometry. This prediction is confirmed experimentally by in vitro reconstitution of the Min system. On the basis of a recently developed theoretical framework for mass-conserving reaction-diffusion systems, we show that the spatiotemporal evolution of the total protein densities on large scales reliably predicts the pattern-forming dynamics. Since conservation laws are inherent in many different physical systems, we believe that our approach can be generalized and contribute to uncover underlying physical principles in multiscale pattern-forming systems.

Introduction

Pattern formation is fundamental for the spatiotemporal organization of biological processes, such as cell division, chemotaxis, and morphogenesis. More than half a century ago, Turing showed theoretically how local interactions (chemical reactions) and diffusion of chemical species can lead to spontaneous spatial patterns [1]. Such reaction–diffusion systems have been successfully used to explain pattern formation phenomena in nature that arise self-organized from a stable homogeneous steady state [2, 3, 4, 5]. The analysis proposed by Turing allows to predict the emergence of patterns with a characteristic length scale as long as the entire dynamics remains in the vicinity of the homogeneous steady state [6]. The validity of Turing's approach has been also tested experimentally for coupled chemical oscillators, and was found to reliably predict the experimental observations, provided that the model parameters are spatially and temporally uniform [7]. Pattern-forming systems, however, are generally heterogeneous and therefore far from homogeneity, and involve multiple spatial and temporal scales. An intriguing example of biological pattern formation is morphogenesis, in which the spatiotemporal patterns of morphogens dictate the future shape of an organism that is orders of magnitude larger than its constituents [4]. On a smaller scale, protein concentration patterns in cells are essential for the spatiotemporal control of cellular processes such as cell division and motility [8, 5, 9]. Protein patterns can exhibit fascinating multiscale characteristics [10] and form in hierarchies of patterns on several scales that affect one another [11].

Such complex multiscale biological processes involve many degrees of freedom at multiple scales, rendering it difficult to analyze them and gain insight into the underlying principles. To make progress on this issue, one needs to use systematic coarse-graining schemes that allow the dynamics to be reduced to the essential degrees of freedom at the relevant time and length scales. Well-known and powerful methods include amplitude equations [6] and the renormalization group theory [12]. Unfortunately, these methods are restricted to the vicinity of special points (a spatially uniform state for amplitude equations and a critical point for the renormalization group, respectively). The Mori-Zwanzig formalism [13] is another important approach which allows to decompose the dynamics of a system into 'fast' and 'slow' variables by means of projection operators. One arrives at a closed set of equations for the slow variables, while the fast variables are treated as noise. One property that all of these methods have in common is that the scales that have been integrated out or eliminated are not *resolved*, and cannot be recovered from the coarse-grained level of description. This is most apparent in the Mori-Zwanzig formalism, where the eliminated degrees of freedom appear effectively as noise terms on the resolved scales. For pattern-forming systems, one is however interested in the patterns on the *unresolved scales*[1] as they usually have a specific function in biological systems. This raises the question of whether it is possible to reconstruct information about the unresolved scales from the dynamics at the resolved scales?

[1] We adapt the term unresolved scales from the computational fluid dynamics literature to refer to the (small) scales that have been integrated out in the coarse-grained description.

We address this general problem in the concrete context of mass–conserving reaction–diffusion (MCRD) systems. Recently, a new theoretical framework for MCRD systems has been introduced [14, 15] that allows one to characterize their dynamics in the highly nonlinear regime. The basic idea is to consider reaction–diffusion system as decomposed into a set of reactive compartments which are spatially coupled by diffusion. For an isolated compartment, one can determine the steady state (*local equilibrium*) and its stability properties which both depend on the total densities within that compartment. Since diffusion causes the lateral redistribution of these total densities, these local equilibria will change over time. This concept of *moving local equilibria* enables one to study the physical mechanisms underlying pattern formation and characterize the dynamics far away from the homogeneous steady state. The fact that one is able to characterize the dynamics far from homogeneity suggests that the *local equilibria theory* may be a promising approach to study heterogeneous systems. We therefore asked whether the ideas from local equilibria theory would be applicable to investigate multiscale patterns?

To pursue this question, we use the Min protein system of *E. coli* which has emerged as a paradigmatic model system for the study of pattern formation in cell biology [16, 17, 18, 19, 20]. Its dynamics is driven by two proteins, MinD and MinE, which cycle between cytosolic and membrane–bound states and interact nonlinearly on the membrane (Fig. 1A). In *E. coli*, these proteins oscillate from cell pole to cell pole and thereby position the cell division machinery to midcell [16, 17]. Studying the Min dynamics in various reconstituted systems has led to the discovery of a rich set of patterns including traveling waves and spirals [18], chaotic patterns [21, 22, 23, 10], "homogeneous pulsing" [24, 25, 26], as well as quasi-stationary labyrinths, spots, and mesh-like patterns [10, 27]. Theoretical analysis of mathematical models has lead to the key insight — and experimentally confirmed prediction — that the average total densities of MinD and MinE and the bulk height are key control parameters for pattern formation in the reconstituted Min system [5, 28]. The rich set of patterns, experimental accessibility *in vitro* and theoretical understanding make the Min-system an ideal candidate to investigate the role of spatial heterogeneity on pattern formation.

Since varying the bulk height affects the local equilibrium state and is a key control parameter for pattern formation [5, 28], we study the Min dynamics in a wedge–shaped geometry with a membrane placed on the bottom surface (Fig. 1B). While there are many distinct ways to introduce large–scale spatial heterogeneities into the system, e.g. by introducing space-dependent kinetic rates, we chose to use a wedge geometry because it is relatively easy to implement experimentally. In numerical simulations, we find that the system exhibits a striking range of transient patterns, that coexist in different spatial regions along the membrane (Movie 1 and Fig. 1C). As time progresses, patterns in different regions change and transition to other patterns.

To characterize these complex dynamics that play out on multiple spatial and temporal scales, we use ideas based on local equilibria theory [14, 15, 8]. We show that one can reconstruct the type and characteristics of patterns on small scales from the local protein mass densities, which are the essential degrees of freedom on large spatial and temporal

scales, i.e. the "hydrodynamic variables" of the system. The key to this reconstruction are correlations between instantaneous, local dispersion relations, calculated from the local mass densities, and the local pattern characteristics. This reconstruction of small-scale features (on *unresolved scales*), together with a coarse-grained description for the mass-redistribution dynamics on large scales allows us to understand and predict the long–term temporal evolution of the system. Thus, the combination of coarse-graining with a (partial) reconstruction of small/fast-scale features is a significant advance as it achieves a greatly reduced description of the system's dynamics without sacrificing the information on the fine scales of the spatiotemporal patters.

A key prediction from our numerical simulations and theoretical analysis is that different pattern types form at different positions along the wedge shaped geometry. To test this prediction experimentally, we performed experiments with a reconstituted Min system in wedge-shaped microfluidic cells. In agreement with the theoretical prediction, we find a range of transient patterns coexisting in different spatial regions along the membrane.

Results

The Min protein system in wedge geometry

Mathematically, the Min-protein dynamics is described by bulk-surface coupled reaction–diffusion equations, which describe the concentrations of cytosolic proteins MinD-ATP, MinD-ADP, and MinE, $\mathbf{c} = (c_{\mathrm{DD}}, c_{\mathrm{DT}}, c_{\mathrm{E}})$, in the bulk volume $\mathcal{V}$, and the concentrations of membrane-bound MinD and MinDE complexes, $\mathbf{m} = (m_{\mathrm{d}}, m_{\mathrm{de}})$, on the surface $\mathcal{S}$. For the wedge geometry, in spatial coordinates $\mathbf{x} = (x, y, z)$, we place the membrane surface (with lateral dimensions $L \times L$) in the $x-y$ plane at $z = 0$ and let the bulk height vary as a linear ramp from H_0 to H_1 along the x-direction (see Fig. 1B).

The dynamics of bulk components $\mathbf{c}(\mathbf{x}, t)$ is governed by the equation

$$\partial_t \mathbf{c}(\mathbf{x}, t) = D_c \nabla^2 \mathbf{c} + \Lambda \mathbf{c}, \tag{1}$$

where D_c denotes the bulk diffusion constant and $\Lambda = \mathrm{diag}(-\lambda, \lambda, 0)$ describes nucleotide exchange of MinD in the bulk. The dynamics of membrane components $\mathbf{m}(x, y, t)$ is constrained to the membrane surface and takes the form:

$$\partial_t \mathbf{m}(x, y, t) = D_m \nabla_{\mathcal{S}}^2 \mathbf{m} + \mathbf{r}(\mathbf{c}|_{z=0}, \mathbf{m}), \tag{2}$$

where D_m is the membrane diffusion constant and $\nabla_{\mathcal{S}}^2 = \partial_x^2 + \partial_y^2$ is the surface Laplacian. The membrane reactions $\mathbf{r}$, which comprise attachment, detachment, and recruitment processes of Min proteins, are specified in the Materials and Methods section.

The dynamics in the bulk and on the surface are coupled by reactive boundary conditions,

$$-D_c \partial_z \mathbf{c}|_{z=0} = \boldsymbol{f}(\mathbf{c}|_{z=0}, \mathbf{m}), \tag{3}$$

that describe the bulk fluxes induced by attachment and detachment of proteins at the membrane (see Materials and Methods). At the remaining boundaries, no-flux boundary

conditions are imposed such that the system is closed. Together, the above dynamics conserve the average mass densities of MinD and MinE:

$$\bar{n}_{\mathrm{D}}\,|\mathcal{V}| = \langle m_{\mathrm{d}} + m_{\mathrm{de}} \rangle_{\mathcal{S}}\,|\mathcal{S}| + \langle c_{\mathrm{D}}\,\rangle_{\mathcal{V}} |\mathcal{V}|\,, \tag{4a}$$

$$\bar{n}_{\mathrm{E}}\,|\mathcal{V}| = \langle m_{\mathrm{de}} \rangle_{\mathcal{S}}\,|\mathcal{S}| + \langle c_{\mathrm{E}} \rangle_{\mathcal{V}}\,|\mathcal{V}|\,, \tag{4b}$$

where $c_{\mathrm{D}} = c_{\mathrm{DD}} + c_{\mathrm{DT}}$ is the total cytosolic MinD concentration; $\langle\cdot\rangle_{\mathcal{S}}$ and $\langle\cdot\rangle_{\mathcal{V}}$ denote the mean on the surface and in the bulk respectively; $|\mathcal{S}|$ and $|\mathcal{V}|$ are the total surface area and bulk volume (see Materials and Methods).

Using finite element (FEM) simulations we investigated the spatiotemporal dynamics of the Min system in wedge geometry. Our simulations show a broad range of different patterns — including traveling waves, standing waves and chaotic patterns — coexisting in different spatial regions of the membrane (see Movie 1 and Fig. 1C). Interestingly, the regions where these patterns are found change over time as the patterns transition from

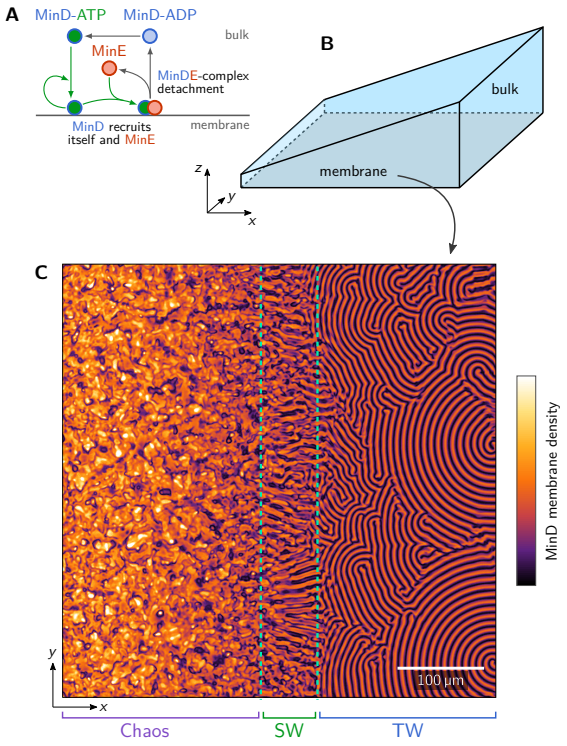

Fig. 1. (*A*) Schematic illustration of the Min-protein reaction network. (*B*) Wedge-geometry with a membrane surface at the bottom plane ($z = 0$) and bulk height $H(x)$ increasing linearly along the x direction. (*C*) Snapshot of the membrane-density of MinD, obtained by numerically simulating the Min dynamics Eqs. 1–3 in the geometry shown in (*B*). One observes regions with chaotic patterns, standing waves (SW, dashed green outline) and traveling waves (TW) along the membrane and at different bulk heights; see Movie 1.

one type to another. For long simulation times, we observe that patterns transition to standing waves, such that the entire domain is covered by a single pattern type in the final steady state. The pattern in steady state depends on the specific choice of parameters, and therefore can be altered by changing the model parameters (Fig. S1 and Movie S1).

Experimental implementation

We tested our theoretical prediction on this multi-scale dynamics in an experimental system consisting of a wedge-shaped microfluidic flow chamber (Fig. 2A). The bottom and top surface of the wedge were covered with a supported lipid bilayer consisting of DOPG:DOPC (30:70 %) which mimics the natural membrane composition of E. coli [29]. The length of the wedge was typically about $8-14\,\mathrm{mm}$ and the width about $3-4\,\mathrm{mm}$. The bulk height range was approximately $2-50\,\mu\mathrm{m}$ (Fig. 2B). Min proteins were distributed in the chamber by rapid injection of a solution containing $1\,\mu\mathrm{M}$ MinD and $1\,\mu\mathrm{M}$ MinE (including 10 % fluorescently labelled MinD and MinE proteins for visualization), together with $5\,\mathrm{mM}$ ATP and an ATP-regeneration system [28].

Figure 2C shows a snapshot of Min protein patterns along the bottom surface of the wedge geometry 30 minutes after injection. The experiments exhibit the same essential hallmarks of multiscale Min protein patterns that we observed in our numerical simulations. In particular, consistent with our simulations, we observe a sequence of distinct spatiotemporal patterns coexisting in different spatial regions of the membrane (Fig. 2C and Movie 2): At regions of low bulk height (approximately between $2-10\,\mu\mathrm{m}$), one typically observes chaotic patterns and standing waves, whereas traveling wave patterns emerge at regions of large bulk height ($>10\,\mu\mathrm{m}$). Furthermore, as in the simulation, we observe a sharp boundary between regions that contain traveling wave patterns and regions that contain rather chaotic and standing wave patterns, and this boundary establishes quickly within a few minutes (Fig. S2 and Movie S2). Overall, the observations provide a striking verification of the height-dependent patterns predicted in the simulations.

There are also some differences between the patterns in the experiment and in our numerical simulations. First, while we observed occasional transitions from one pattern into another in our experiments (Fig. S3 and Movie S3), these transitions occurred frequently and were more pronounced in the simulations. This is explained by the lateral length of the experimental setup, that is about an order of magnitude larger as compared to the simulation setup, which is the main reason why we observe more frequent transitions between different patterns in the simulations, as will become clear later. Second, in contrast to the simulations, we noticed some homogeneous oscillations in the experiments, which are characterized by large (homogeneous) density patches on the membrane (typically few hundred micrometers in size) that oscillate with time (Figs. S3– S4 and Movies S3– S5). We attribute this difference to the following: Due to the fabrication method of the microfluidic flow chamber, both the bottom and top surface of the wedge were covered with a supported lipid bilayer. In recent work, it has been shown that membrane-to-membrane crosstalk (i.e., between top and bottom surface) is responsible for the emergence of homogeneous oscillations [28]. In our simulations, however, we assume that Min proteins can only bind

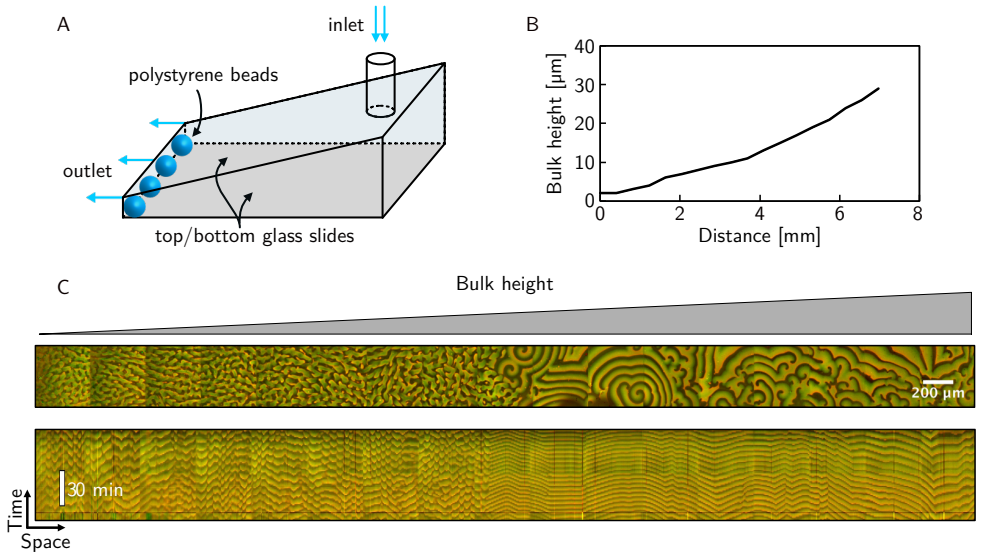

Fig. 2. Experimentally observed Min patterns in a wedge flow cell. (*A*) Schematic presentation of the experimental setup. Both, the bottom and the top surface (glass slides) are covered with a lipid bilayer. (*B*) Measurement of the bulk height profile of the flow cell versus distance along the lateral length of the wedge. The height was measured microscopically by z-stacks at multiple spots. (*C*) Snapshot of the Min pattern along the wedge, the picture was obtained by stitching individual adjacent images. Shown is a merge of MinD (green) and MinE (red) channels. The bottom figure shows a kymograph along the white dashed line as shown in the top figure.

to the bottom membrane, which explains why we do not observe homogeneous oscillations.

Taken together, we have a system that exhibits a fascinatingly rich transient dynamics and involves patterns and transitions between them on multiple spatial and temporal scales. We are therefore left with the key question: Can we explain the cause why different patterns form in different spatial regions and how they transition from one to another over time? Moreover, is it possible to identify and reduce the system to its essential degrees of freedom?

Instantaneous, local dispersion relations predict patterns

In previous theoretical work [14], the reconstituted Min system was investigated in a two-dimensional rectangular geometry representing a slice through a three-dimensional *in vitro* system, where the rectangle's bottom edge represents the membrane surface (Fig. 3A). Depending on the total densities of Min proteins, $\bar{n}_{\mathrm{D}}$ and $\bar{n}_{\mathrm{E}}$ and the bulk height H, it was shown that the system establishes a variety of different patterns on the membrane such as chaos, standing waves, and traveling waves [14, 28].

The analysis of pattern-forming systems usually starts with calculating the homogeneous steady state $\mathbf{m}^*(H, \bar{n}_{\mathrm{D}}, \bar{n}_{\mathrm{E}})$, $\mathbf{c}^*(H, \bar{n}_{\mathrm{D}}, \bar{n}_{\mathrm{E}})$ and determining its stability. In particular, a linear stability analysis of these homogeneous steady states yields the *dispersion relation*

that informs about the growth rate $\sigma(q)$ of perturbations with a certain wavenumber q (Fig. 2B).

In general, from the dispersion relation one can only determine the dynamics in the vicinity of the homogeneous steady state. However, careful analysis of numerical simulations of the Min system have interestingly also revealed a strong one-to-one correlation between the dispersion relation and fully developed patterns in the highly nonlinear regime [14]: A *commensurability criterion* between the unstable mode with the shortest wavelength $q_{\max}$ and the fastest growing mode q^* has been found that dictates the pattern type (Fig. 3C–E). In short, it has been shown that $q_{\max}/q^* < 2$ coincides with the regime of chemical turbulence, whereas for $q_{\max}/q^* > 2$ the system exhibits ordered patterns (standing/traveling waves) [14]. Standing wave patterns are found close to the commensurability transition $q_{\max}/q^* \gtrsim 2$, while traveling waves are found further away from the threshold [14]. Since the form of the dispersion relation, and with it the commensurability ratio, depends on parameters, this suggests that pattern formation is sensitive to the value of the total densities and bulk height. Here we use this observed one-to-one correspondence between the dispersion relation and patterns in the nonlinear regime to investigate pattern formation in our system.

Let us consider the wedge as dissected into a collection of two-dimensional slices along the direction of constant bulk height. Each slice corresponds to a rectangular geometry with a bulk height that depends on the position of the slice in the wedge (see Fig. 3B). While the bulk height is a fixed parameter for each slice, the average total densities $\langle \tilde{n}_{\mathrm{D,E}} \rangle_y(t, x)$ (Materials and Methods) in each slice are variable and depend on slice position x and time t as the diffusive coupling between the slices redistributes mass. This generalizes previous findings Ref. [14], where a two-dimensional geometry, with a rectangular bulk and a membrane at the bottom edge (corresponding to a single, isolated slice through the wedge geometry) was studied. To test whether the commensurability relation $q_{\max}/q^*$ also correlates with the pattern type in the wedge geometry, we extracted the average total densities in each slice as a function of time from the numerical simulation. Based on these densities we then performed the analysis illustrated in Fig. 3: We calculated the *instantaneous* dispersion relation in each slice and extracted the the ratio $q_{\max}/q^*$ as a function of slice position x and time t. The resulting pattern-type prediction is shown in the space-time plot (kymograph) in Fig. 4A. Figure 4B shows the ratio $q_{\max}/q^*$ as a function of slice position x for a set of representative times (cf. Fig. 3D). The pattern-type prediction Fig. 4A is then obtained from these ratios via the mapping shown in Fig. 3D,E.

We find that this prediction correlates well with the patterns observed in the full numerical simulation (Fig. 4C,D and Movie 3). In particular, the temporally changing position $x_{\mathrm{crit}}(t)$ $q_{\max}/q^* = 2$ (indicated by the green arrows and dashed lines in Fig. 4B and C) agrees with the position along the wedge where traveling wave patterns transition to chaotic patterns. In the vicinity of $x_{\mathrm{crit}}(t)$ we observe a band of standing waves as expected from the "commensurability criterion" [14]. Since the the ratio $q_{\max}/q^* = 2$ and with it the $x_{\mathrm{crit}}(t)$ are entirely determined by the slice-averaged masses $\langle \tilde{n}_{\mathrm{D,E}} \rangle_y(x, t)$, we conclude that these masses are the essential degrees of freedom of the system on large scales.

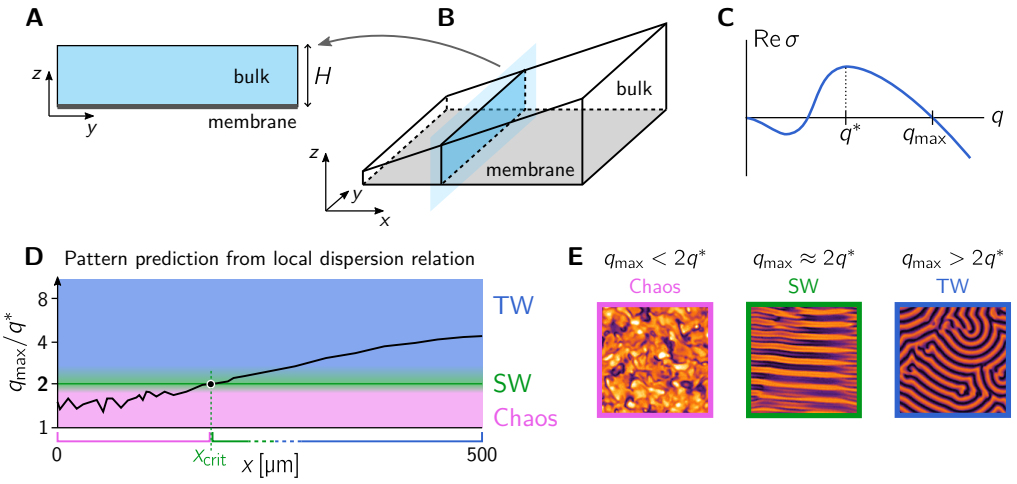

Fig. 3. (*A*) Rectangular geometry with membrane at the bottom edge representing a slice through the three-dimensional in vitro system. (*B*) A slice through the wedge geometry. For each such slice, at a given instance in time, we calculate the instantaneous total densities, averaged along its length $\langle \tilde{n}_{\mathrm{D,E}} \rangle_y(t,x)$, from the numerical simulation data. From these slice-averaged total densities, we can then calculate the corresponding local homogeneous steady state and its dispersion relation. (*C*) *Dispersion relation* with fastest growing mode q^* and right edge of the band of unstable modes q_{max} indicated. The ratio q_{max}/q^* has been empirically found to correlate with the type of the fully developed pattern, with a sharp transition from chaotic patterns for $q_{\mathrm{max}}/q^* < 2$ to ordered patterns for $q_{\mathrm{max}}/q^* > 2$. Close to the transition, standing waves are found, while travelling waves form for larger ratios q_{max}/q^* [14]. (*D*) Mode ratio q_{max}/q^* as a function of the slice position x for a given instance in time. The background shading indicates the type of pattern expected from the "commensurability criterion." (*E*) Representative snapshots of the three distinct pattern types: spatiotemporal chaos, standing waves (SW) and traveling waves (TW).

Next, we ask whether one can find an approximate coarse-grained dynamics for these redistributed masses. Such a description would enable us to predict the time evolution of the redistributed masses independently from the full numerical simulations. One can then use the commensurability criterion to predict the pattern types that will form in different spatial regions as a function of the redistributed masses. In the next section we will show how one can find such a description.

Large-scale dynamics is driven by redistribution of mass

In general, mass redistribution between different spatial regions of the wedge is caused by diffusive fluxes due to concentration gradients. Similar as in the previous section, we consider here the redistribution of mass between slices along the wedge (Fig. 3B). Since membrane diffusion is by two orders of magnitude slower than bulk diffusion it may be ne-

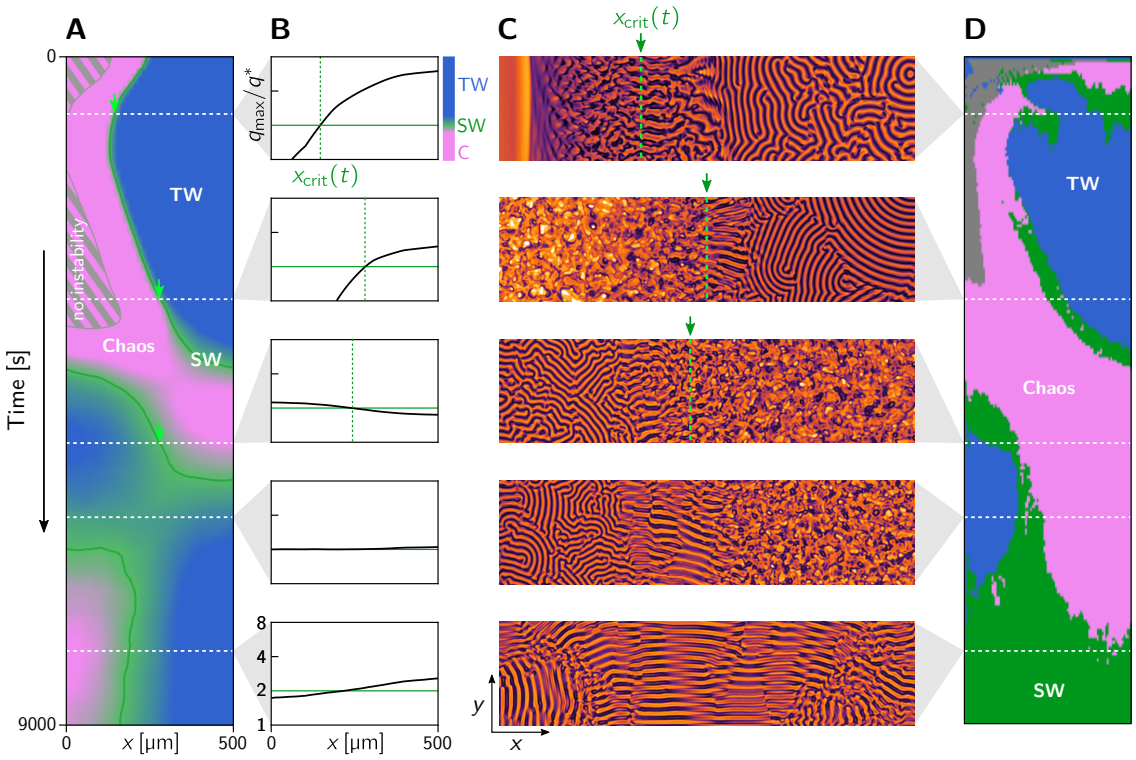

Fig. 4. (*A*) Kymograph showing the pattern-type prediction from the commensurability criterion (cf. Fig. 3D). The green line shows $x_{\mathrm{crit}}(t)$ where $q_{\mathsf{max}}/q^* = 2$, indicating the transition from chaotic to ordered patterns. Green arrows mark the position $x_{\mathrm{crit}}(t)$ for the times indicated by dashed white lines. (*B*) Plots of the mode ratio q_{max}/q^*, determined from the local dispersion relation, as a function of spatial position x for several representative times (dashed white lines in (A)). In the second to last row, the entire domain is near the critical ratio $q_{\mathsf{max}}/q^* = 2$, predicting the global emergence of standing waves (see last row). (*C*) Snapshots of the membrane patterns (MinD density, cf. Fig. 1) from the full numerical simulation. The green dashed line indicates $x_{\mathrm{crit}}(t)$. Note the standing wave patterns found near $x_{\mathrm{crit}}(t)$. Their fronts are aligned along the bulk height gradient such that the sequence of wavenodes lies on lines of constant bulk height. (*D*) Machine-learning based pattern classification using *ilastik* [30] (see Materials and Methods).

glected, such that redistribution of protein mass between slices is governed by bulk diffusion alone (Materials and Methods)

$$\partial_t \langle n_i \rangle_{y,z}(x,t) \approx D_c \langle \partial_x^2 c_i \rangle_{y,z} + D_c \frac{\partial_x H(x)}{H(x)} \langle \partial_x c_i \rangle_{y,z}, \tag{5}$$

for $i = \mathrm{D}, \mathrm{E}$. Here, the second term accounts for the spatial variation of the bulk height, and thus the different volumes of neighboring slices between which the diffusive flux $D_c \langle \partial_x c_i \rangle_{y,z}$

redistributes mass. This can be seen by rewriting Eq. (5) in the form of a continuity equation

$$\partial_t \big[H(x) \cdot \langle n_i \rangle_{y,z}(x,t)\big] \approx -\partial_x \big[H(x) \cdot J_i^{\mathrm{diff}}\big] \tag{6}$$

with the diffusive fluxes given by $J_i^{\mathrm{diff}} := -D_c \langle \partial_x c_i \rangle_{y,z}$. Since the area of slices increases along the positive $x-$direction, the diffusive fluxes J_i^{diff} on the right-hand side of Eq. (6) are rescaled by the bulk height $H(x)$. These equations seem to be simple, but unfortunately they are not closed, since the slice-averaged cytosolic densities $\langle c_i \rangle_{y,z}(x,t)$ appear on the right hand side.

We are interested in the dynamics of $\langle n_i \rangle_{y,z}$ on timescales much longer than typical oscillation periods of the patterns. Therefore, following the intuition gained from previous works on MCRD systems [15, 31], we assume that one can approximate the slice-averaged cytosol concentrations by the homogeneous steady-state concentration in each slice

$$\langle c_i \rangle_{y,z}(x,t) \approx c_i^*(x,t) := c_i^*\big(H(x), \langle n_{\mathrm{D}} \rangle_{y,z}, \langle n_{\mathrm{E}} \rangle_{y,z}\big). \tag{7}$$

This assumes that the spatial average over many wavelengths in y-direction is well approximated by the instantaneous homogeneous steady state in a slice. These steady state

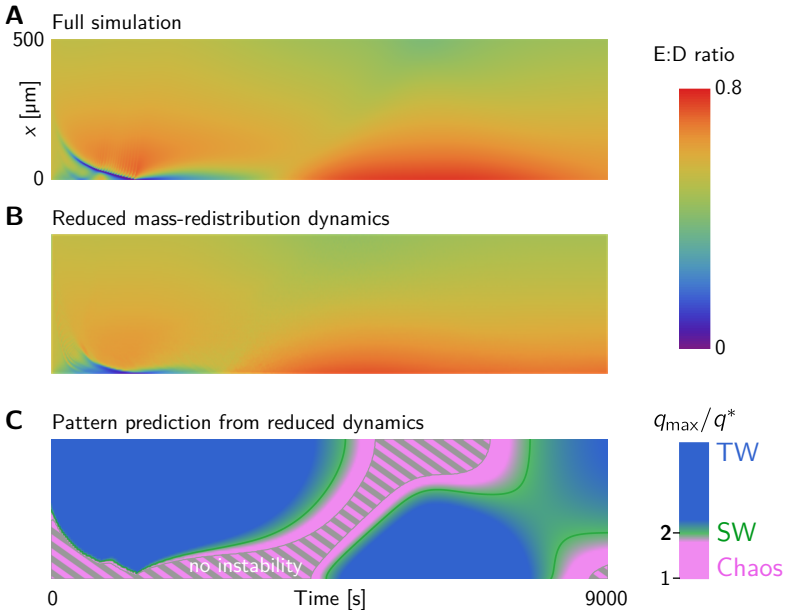

Fig. 5. (*A*,*B*) Kymographs showing the total-density ratio of MinE to MinD (E:D ratio) from the full numerical simulation (*A*) and from local-equilibria based reduced dynamics (*B*). (*C*) Kymograph showing the pattern-type prediction using the commensurability criterion based on the total densities from the reduced dynamics. Note the excellent qualitative agreement to the pattern-type prediction based on total densities from the full numerical simulation in Fig. 4A.

concentrations only depend on the slices bulk height $H(x)$ and the slice-averaged total densities $\langle n_i \rangle_{y,z}(x,t)$. Thus, the above approximation yields a closed set of equations for the mass-densities

$$\partial_t \langle n_i \rangle_{y,z}(x,t) \approx D_c \partial_x^2 c_i^*(x,t) + D_c \frac{\partial_x H(x)}{H(x)} \partial_x c_i^*(x,t). \tag{8}$$

We will call this the *reduced dynamics* in the following. Since the homogeneous steady states may also undergo a saddle-node bifurcation, characterized by the emergence of three steady states emerge (two stable, one unstable), this may lead to discontinuities in c_i^*. To regularize the dynamics, c_i is not set identical to c_i^* but relaxes towards it on a fast timescale (see SI for details).

Given the initial densities $\langle n_i \rangle_{y,z}(x,0)$, one can numerically solve the reduced dynamics Eq. (8) to predict the entire time evolution of the slice-averaged masses and hence the dispersion relation at each point along the $x-$direction. Figure 5C shows the regional pattern types predicted from the reduced dynamics. We find good qualitative agreement for the distribution and transition of patterns as observed in the numerical simulations (cf. Fig. 4A). The main difference to the full numerical simulations is a slight quantitative deviation in the timescale, where the mass redistribution predicted by Eq. (8) is slightly slower compared to the full numerical simulation. We also note that the reduced dynamics predicts a larger region of no instabilities as compared to the numerical simulations (cf. Figs. 4A and 5C). This is, on one hand, because the chaotic regime is rather narrow and close to the regime for which the dispersion relation predicts no instability (cf. Figs. 3D and 4B). In addition, since the patterns emerge from a subcritical bifurcation [14] (a generic property of mass-conserving systems [15]), large amplitude patterns can be excited and maintained even below the instability threshold.

Figure 5A,B compare the time evolution of the slice-averaged total densities from the full numerical simulation and the solution obtained from the reduced dynamics. The colors in the kymographs indicate the total density ratio of MinE and MinD (short, E:D ratio), which is a key control parameter in the Min-protein dynamics [14].

Discussion

Multiscale patterns in biological systems often emerge from hierarchical systems, which are organized in a modular fashion. Each level of the hierarchy instructs dynamics on the next level which operates on a smaller spatial scale. For instance, along developmental trajectories of many organisms, upstream patterns such as maternal gradients instruct downstream gene-expression patterns on increasingly smaller scales [32, 11]. Importantly, on each level of the hierarchy, there is a clean separation between (spatially varying) control parameters and dynamical variables.

In contrast, in the system we have studied here, there is no such separation as the globally conserved total densities play a dual role: they are both dynamical variables and act as control parameters [14, 15]. Building on this key feature has allowed us to explain and predict the intriguingly complex patterns found in large-scale numerical simulations. The values of the total densities of MinD and MinE locally control the pattern type: we showed

that a "regional dispersion relation" calculated from the regional average densities reliably predicts the pattern type. At the same time, concentration gradients in the bulk drive mass redistribution of MinD and MinE. Therefore, the total densities are hydrodynamic variables on large scales which control pattern formation on small scales. This separation of scales enabled us to derive a reduced dynamics for the total densities on large spatial and temporal scales which predicts the long-term dynamics of the system.

Notably, the dual role of total densities as dynamic variables and control parameters also plays out at the small scale of the patterns themselves [14, 15]. Here, instantaneous *local* total densities control *local* equilibria and their stability, which serve as proxies for the local dynamics. The local dynamics cause gradients, which drive diffusive redistribution of the total densities—in turn causing changes in the local dynamics. In the Min system, this point of view has led to a detailed understanding of the emergence of chaos near onset and of the transition to standing and traveling waves [14]. From a general perspective, the concept of local equilibria controlled by total local densities is at the core of a number of recent theoretical advances in the field of mass-conserving, pattern-forming systems [15, 31, 33, 8].

In addition to the dynamically changing total densities, the bulk height is also a (fixed) heterogeneous control parameter in our system. The bulk height (or more generally volume-to-surface ratio) is an important control parameter for bulk-surface coupled pattern-forming systems [14, 28]. Here, the bulk height gradient of the wedge serves to induce spatiotemporal heterogeneities in the total densities. Alternatively, one could induce heterogeneities in the total densities via spatial gradients of the kinetic rates or by imposing a heterogeneous initial condition in the total densities. However, these alternatives are difficult to realize experimentally in a reproducible and controlled manner, which is the main reason why we chose the wedge setup in this work. In a third scenario, large-scale gradients in the densities may also emerge spontaneously and be maintained in the absence of "external" heterogeneities. This is the case in systems with a long wavelength instability, such as vibrated granular media [34, 35].

Since conservation laws are ubiquitous in many physical systems, we believe that our approach can be generalized to a broad class of multiscale pattern-forming systems. For instance, mass conservation is inherent to particle–based active matter systems. The local particle density controls emergent orientational order, i.e. local symmetry breaking [36, 37, 38]. In turn, orientational order controls mass redistribution due to the particles' self-propulsion. Thus, the particle density again plays a dual role as a control parameter and a dynamic variable [38, 39, 40]. The dynamic interplay of mass redistribution and orientational order has been shown to give rise to coexistence of different macroscopic order (polar flocks, nematic lanes) and the interconversion between them [38], not unlike the coexistence and interconversion of different patterns we found for the reaction–diffusion system studied in this work. One way to induce spatial heterogeneities in these systems is to introduce a gradient of signaling chemicals (chemoattractants) that affect the local velocity of active particles. This would dynamically lead to redistribution of the particle densities on large scales. Since the particle densities, in turn, are themselves control parameters locally, non-trivial multiscale dynamics may emerge in such a setup. Exploring the effects of such gradients in active

matter systems could be therefore an exciting task for future research.

Beside mass-conserving systems, there is also a number of studies on Turing patterns in domains with spatially varying model parameters (kinetic rates [41, 42] or diffusion coefficients [43]). For one-dimensional models, one can derive an instability criterion for distinct sections of the domain by determining the (local) growth rates of perturbations [41]. This is similar to our approach, where we identified (regional) patterns from the dispersion relation and the resulting commensurability criterion in each slice along the wedge geometry. In these studies on classical Turing models, there is a strict separation between (heterogeneous) control parameters and dynamical variables, i.e. they can be seen as hierarchical systems like those discussed above. Going forward, it would be interesting to dynamically couple control parameters in these models to another pattern-forming system in order to drive transient multiscale patterns, similar to this work.

Our work relied on a relation between regional parameters (average total densities) and regional pattern types. A systematic understanding of this commensurability criterion is still lacking, leaving an interesting task for future research. As an alternative one might go in the opposite direction forgoing mechanistic insight and instead relying on machine learning, for instance. A large number of small scale simulations could be used as training data to "learn" a relationship between parameters and pattern type. This learned relationship could then be combined with an effective dynamics describing the redistribution of mass, where the masses enter as spatiotemporally varying parameters. Specifically one could train a neural network to learn an relation between the slice-averaged total densities and slice-averaged cytosolic densities that can be substituted in Eq. (6) to obtain a closed set of equations for the redistribution of mass between slices. Such "physics-informed neural networks" have received significant attention in recent years [44, 45, 46]. Mass conservation is an important and ubiquitous physical constraint that might help to further develop physics-informed machine learning approaches in future work.

On a broader perspective, our work showed that spatiotemporal patterns at small scales can be reconstructed from the reduced dynamics at large length and time scales (mass redistribution). We believe that our approach can be generalized and applied to other multiscale systems with an underlying conservation law, such as transport processes in porous media, combustion, and cell migration, to name a few examples. The possibility of obtaining information about the dynamics at the small scales from the coarse-grained description at large scales opens a new avenue to gain insight into the underlying principles of such systems.

Materials and Methods

Mathematical model

We adopt the Min "skeleton model" introduced in Refs. [47, 48, 5] which is known to qualitatively reproduce Min patterns *in vivo* and *in vitro* [48, 5, 28]. The governing equations are given in the main text, Eqs. [1]–[3]. The membrane reactions are

$$\mathbf{r} = \left[r_{\mathrm{D}}^{\mathrm{on}} - r_{\mathrm{E}}^{\mathrm{on}}, r_{\mathrm{E}}^{\mathrm{on}} - r_{\mathrm{DE}}^{\mathrm{off}}\right]^{\top}, \tag{9}$$

with

$$r_{\mathrm{D}}^{\mathrm{on}} = (k_{\mathrm{D}} + k_{\mathrm{dD}} m_{\mathrm{d}}) c_{\mathrm{DT}}\,, \tag{10a}$$

$$r_{\mathrm{E}}^{\mathrm{on}} = k_{\mathrm{dE}} m_{\mathrm{d}} c_{\mathrm{E}}\,, \tag{10b}$$

$$r_{\mathrm{DE}}^{\mathrm{off}} = k_{\mathrm{de}} m_{\mathrm{de}}\,. \tag{10c}$$

The reaction terms account for MinD attachment and self-recruitment to the membrane, MinE recruitment by MinD, and dissociation of MinDE complexes with subsequent detachment of both proteins into the cytosol, respectively. Coupling between cytosol and membrane is established by reactive boundary conditions at the membrane [cf. Eq. (3)]. The boundary fluxes are given by

$$\boldsymbol{f} = \left[r_{\mathrm{DE}}^{\mathrm{off}}, -r_{\mathrm{D}}^{\mathrm{on}}, r_{\mathrm{DE}}^{\mathrm{off}} - r_{\mathrm{E}}^{\mathrm{on}}\right]^{\top}, \tag{11}$$

which follows from mass conservation. For analytical caclulations we adapt the following change of variables as it is more convenient: We describe the bulk dynamics of MinD in terms of the variables $c_{\mathrm{D}} = c_{\mathrm{DD}} + c_{\mathrm{DT}}$ and c_{DD}, i.e. in this case one defines the bulk concentration vector $\mathbf{c} = (c_{\mathrm{D}}, c_{\mathrm{DD}}, c_{\mathrm{E}})$. The membrane reaction in Eq. (10a) is then slightly modified by substituting $c_{\mathrm{DT}} = c_{\mathrm{D}} - c_{\mathrm{DD}}$, and the boundary fluxes are given by

$$\boldsymbol{f} = \left[-r_{\mathrm{D}}^{\mathrm{on}}, r_{\mathrm{DE}}^{\mathrm{off}}, r_{\mathrm{DE}}^{\mathrm{off}} - r_{\mathrm{E}}^{\mathrm{on}}\right]^{\top}. \tag{12}$$

The model parameters used in this study are summarized in Table 1.

Table 1. Min model parameters

Parameter	Symbol	Value
Bulk diffusion	D_c	$60\,\mu\mathrm{m}^2\,\mathrm{s}^{-1}$
Membrane diffusion	D_m	$0.013\,\mu\mathrm{m}^2\,\mathrm{s}^{-1}$
Average total MinD density	$\bar{n}_{\mathrm{D}}$	$665\,\mu\mathrm{m}^{-3}$
Aveage total MinE density	$\bar{n}_{\mathrm{E}}$	$410\,\mu\mathrm{m}^{-3}$
Attachment rate	k_{D}	$0.065\,\mu\mathrm{m}\,\mathrm{s}^{-1}$
MinD recruitment rate	k_{dD}	$0.098\,\mu\mathrm{m}^3\,\mathrm{s}^{-1}$
MinE recruitment rate	k_{dE}	$0.126\,\mu\mathrm{m}^3\,\mathrm{s}^{-1}$
MinDE dissociation rate	k_{de}	$0.34\,\mathrm{s}^{-1}$
Nucleotide exchange	λ	$6\,\mathrm{s}^{-1}$

Numerical simulation

To investigate the dynamics of the system, we performed 3D finite element (FEM) simulations using the commercially available software *COMSOL Multiphysics v5.6*. Numerical simulations were performed for a wedge geometry with lateral length $L = 500\,\mu\text{m}$ and bulk height $H(x)$ linearly increasing from $H_0 = 5\,\mu\text{m}$ to $H_1 = 50\,\mu\text{m}$. The simulation was initialized with the Min proteins uniformly distributed in the bulk and a small random spatial perturbation around this uniform state.

Homogeneous steady state and dispersion relation

The homogeneous steady state concentrations, $(\mathbf{c}^*|_{z=0}(H, \bar{n}_\text{D}, \bar{n}_\text{E}),\ \mathbf{m}^*(H, \bar{n}_\text{D}, \bar{n}_\text{E}))$ are obtained from the stationary solutions of Eqs. (1)–(3) together with the mass conservation condition Eq. (4):

$$\begin{cases} \mathbf{r}(\mathbf{c}^*|_{z=0}, \mathbf{m}^*) = \mathbf{0}, \\ \boldsymbol{f}\left(\mathbf{c}^*|_{z=0}, \mathbf{m}^*\right) = \boldsymbol{\Phi}, \\ c^*_\text{D}|_{z=0} + (m^*_\text{d} + m^*_\text{de})/H = \bar{n}_\text{D}, \\ c^*_\text{E}|_{z=0} + m^*_\text{de}/H = \bar{n}_\text{E}, \end{cases} \tag{13}$$

where $\boldsymbol{\Phi}$ denotes the steady state fluxes at the membrane, given by:

$$\boldsymbol{\Phi} = [0, \phi, 0]^\top, \tag{14a}$$

$$\phi := \sqrt{D_c \lambda}\, \tanh\left(\sqrt{\lambda/D_c}\, H\right)\, c^*_\text{DD}|_{z=0}. \tag{14b}$$

A concise derivation of these equations and how they can be solved is provided in the Supplementary Information. For a thorough presentation of the linear stability analysis of the Min system in a 2D rectangular geometry we refer to the Supplementary Informations of Refs. [14] and [28].

Operators for spatial averaging

The operators used throughout this study to calculate mean values of densities on the membrane and in the cytosol are defined as follows:

$$\langle m \rangle_\mathcal{S} := |\mathcal{S}|^{-1} \int_\mathcal{S} \mathrm{d}x\mathrm{d}y\, m, \tag{15a}$$

$$\langle c \rangle_\mathcal{V} := |\mathcal{V}|^{-1} \int_\mathcal{S} \mathrm{d}x\mathrm{d}y \int_0^{H(x)} \mathrm{d}z\, c, \tag{15b}$$

$$\langle \cdot \rangle_y := \frac{1}{L} \int_0^L \mathrm{d}y\, (\cdot), \tag{15c}$$

$$\langle \cdot \rangle_{y,z} := \frac{1}{H(x)} \int_0^{H(x)} \mathrm{d}z\, \langle \cdot \rangle_y, \tag{15d}$$

where the membrane surface area and the bulk volume for the wedge geometry are explicitly given by $|\mathcal{S}| = L^2$ and $|\mathcal{V}| = L^2\,(H_0 + H_1)/2$.

Instantaneous total densities *at* the membrane

Since only cytosolic proteins in close proximity to the membrane participate in the nonlinear dynamics at the membrane, we define instantaneous total densities at the membrane:

$$\tilde{n}_{\mathrm{D}}(x,y,t) := \frac{1}{H(x)}(m_{\mathrm{d}} + m_{\mathrm{de}}) + c_{\mathrm{D}}|_{z=0}\,, \tag{16a}$$

$$\tilde{n}_{\mathrm{E}}(x,y,t) := \frac{1}{H(x)} m_{\mathrm{de}} + c_{\mathrm{E}}|_{z=0}\,. \tag{16b}$$

We further averaged these densities along the y–direction to obtain the the slice-averaged total densities $\langle \tilde{n}_{\mathrm{D,E}} \rangle_y(x,t)$. Note that the length of a slice is much larger than the typical pattern wavelength, which also permits to approximate the slice-averaged mass at the membrane by the vertically averaged mass: $\langle \tilde{n}_i \rangle_y(x,t) \approx \langle n_i \rangle_{y,z}(x,t)$ (see Ref. [14]). This is because the local deviations $\tilde{n}_i - \langle n_i \rangle_z$ largely cancel when averaging over the pattern wavelength.

Mass redistribution dynamics

Here, we provide more details on the derivation of the mass redistribution dynamics Eq. (6). For specificity, we present the calculation for MinD. The calculation for MinE works along the same lines. Our starting point is the slice averaged total MinD density:

$$\langle n_{\mathrm{D}} \rangle_{y,z}(x,t) := \frac{1}{H(x)} \left\langle m_{\mathrm{d}} + m_{\mathrm{de}} + \int_0^{H(x)} \mathrm{d}z\, c_{\mathrm{D}} \right\rangle_y . \tag{17}$$

The time evolution of this quantity then follows from Eq. (1) and Eq. (2):

$$\begin{aligned} H(x)\, \partial_t \langle n_{\mathrm{D}} \rangle_{y,z}(x,t) = {} & D_m \partial_x^2 \langle m_{\mathrm{d}} + m_{\mathrm{de}} \rangle_y \\ & + D_c \partial_z \langle c_{\mathrm{D}} \rangle_y \big|_{z=H(x)} + \int_0^{H(x)} \mathrm{d}z\, D_c \partial_x^2 \langle c_{\mathrm{D}} \rangle_y, \end{aligned} \tag{18}$$

where we used the reactive boundary condition Eq. (3) to rewrite the integral:

$$\begin{aligned} \int_0^{H(x)} \mathrm{d}z\, D_c \partial_z^2 c_{\mathrm{D}} &= D_c \partial_z c_{\mathrm{D}} \big|_{z=H(x)} - D_c \partial_z c_{\mathrm{D}} \big|_{z=0} \\ &= D_c \partial_z c_{\mathrm{D}} \big|_{z=H(x)} + r_{\mathrm{DE}}^{\mathrm{off}} - r_{\mathrm{D}}^{\mathrm{on}}. \end{aligned} \tag{19}$$

Note that due to mass-conservation the reaction terms at the membrane cancel.

Since the system is closed, the boundary condition at the inclined top surface of the wedge reads $\mathbf{n} \cdot \nabla c_{\mathrm{D}}|_{z=H(x)} = 0$, where $\mathbf{n} \propto (-\partial_x H, 0, 1)$ is the outward normal vector at the top surface. Writing out the boundary condition explicitly, we find that:

$$\partial_z c_{\mathrm{D}}|_{z=H(x)} = (\partial_x H)\, \partial_x c_{\mathrm{D}}|_{z=H(x)}. \tag{20}$$

To proceed, we substitute the relation above into Eq. (18) and slightly rewrite the resulting equation by applying the chain rule:

$$H(x)\,\partial_t\langle n_{\mathrm{D}}\rangle_{y,z}(x,t) = D_m\partial_x^2\langle m_{\mathrm{d}}+m_{\mathrm{de}}\rangle_y + \partial_x \underbrace{\int_0^{H(x)} \mathrm{d}z\, D_c\partial_x\langle c_{\mathrm{D}}\rangle_y}_{=:\,-H(x)J_{\mathrm{D}}(x)}. \tag{21}$$

Here, the first term describes diffusion of the averaged membrane concentrations. The integral on the right describes diffusion of the averaged cytosolic densities, where we defined the diffusive flux $J_{\mathrm{D}} = -D_c\langle\partial_x c_D\rangle_{y,z}$. The factor $H(x)$ in the cytosolic diffusion term accounts for the increasing area of the slice along the positive x–direction.

Since protein diffusion on the membrane is much smaller than cytosolic diffusion $D_m \ll D_c$ [49, 50], one can neglect membrane diffusion to arrive at the result shown in the main text (Eq. (6)). For completeness, note that Eq. (21) (without membrane diffusion) can be recast as

$$\begin{aligned}\partial_t\langle n_{\mathrm{D}}\rangle_{y,z}(x,t) &\approx \frac{1}{H(x)}\,\partial_x\int_0^{H(x)}\mathrm{d}z\, D_c\partial_x\langle c_{\mathrm{D}}\rangle_y,\\ &= D_c\partial_x\langle\partial_x c_{\mathrm{D}}\rangle_{y,z} + D_c\frac{\partial_x H(x)}{H(x)}\langle\partial_x c_{\mathrm{D}}\rangle_{y,z},\end{aligned} \tag{22}$$

which is the form given in Eq. (5) in the main text.

Machine-learning based pattern classification

We used the pixel classifier provided by the software *ilastik* [30]. The classifier was trained based on a few representative snapshots, by manually marking areas where the pattern type (no pattern, chaos, standing wave, or traveling wave) is easily identified by visual inspection. The trained classifier then yields probabilities for each pattern type at each pixel. The classifier was applied to snapshots in 20 s intervals. This data was then downsampled and averaged over slices to yield an x–t space time map of pattern probabilities. To render the kymograph in Fig. 4D each pixel was colored based on the most probable pattern.

Preparation of the wedge flow cell

The microfluidic wedge chambers were prepared using two rectangular cover slips (bottom one of dimensions 22/50 mm, and top one of dimensions 5/30 mm). Close to one of the short edges of a top glass a tiny inlet hole was drilled using a sandblaster. Cover slips were cleaned in 1 M KOH for 1 h followed by a methanol bath for 10 min in a sonicator bath. Surfaces of the cover slips were activated with oxygen plasma for 20 s, using oxygen plasma PREEN I (Plasmatic System, Inc.) with a O2 flow rate of 1 SCFH. Furthermore, a small PDMS slab with a 0.3 mm hole was attached on to the top glass slide, such that it matches the hole in the PDMS glass slide and a metal connector was inserted in the hole for connecting the syringe pump. Tilt of the top glass slide was achieved by placing a piece of aluminum

foil between the top and bottom slide at the end, with the largest height between top and bottom at the side of the inlet. At the opposite side with the smallest distance between top and bottom slide, 2 µm polystyrene beads that were deposited on the bottom slide provided an outlet and prevent a collapse of the top and bottom slides (see Fig. 2). The lateral sides of the microchamber were sealed with a two-component epoxy resin leaving the short edge at the low height-side open for liquid flow (Fig. S4). The microfluidic cell was then filled with a solution of small unilamellar vesicles (SUVs) through an injection tube at the inlet of the PDMS slab and incubated for 30 min at 30 °C–yielding full lipid membrane coverage of the bottom and top slides. SUVs were prepared as described in Ref. [28]. Subsequently, the flow cell was thoroughly washed with a buffer to remove excess SUVs and Min protein experiments were started.

Observation of Min patterns

We purified the Min proteins based on the method proposed in Ref. [51]. Injection of Min proteins into the flow cells was performed through a syringe pump containing a solution of 0.8 M MinD, 0.2 mM MinD-Cy3, 0.8 mM MinE, 0.2 mM MinE-Cy5, 5 mM ATP, 4 mM phosphoenolpyruvate, 0.01 mg/ml pyruvate kinase, 25 mM Tris-HCl (pH 7.5), 150 mM KCl and 5 mM MgCl2. To ensure that all of the buffer solution in the microdevice is replaced by the protein solution, we chose a volume of the protein solution that was 50 times larger than the volume in the microdevice. During the filling process of the microdevice, the enire solution was rapidly injected (in 5 s) to prevent protein accumulation on the membrane.

For the generation of the fluorescence images, we used the following equipment: Olympus IX-81 inverted microscope equipped with an Andor Revolution XD spinning disk system with FRAPPA, illumination and detection system Andor Revolution and Yokogawa CSU X1, EM-CCD Andor iXon X3 DU897 camera, motorized x-y stage and a z-piezo stage, using a 20x objective (UPlansApo, NA 0.85, oil immersion). Imaging of MinD-Cy3 and MinE-Cy5 was performed with laser spectral lines at 561 nm and 640 nm, respectively, and we further used a 617/73 band-pass filter as well as a 690 long-pass filter. We imaged several uniformly sized regions at intervals of 30 s or 60 s along the lateral length of the wedge setup. To exclude membrane imperfections that may have arisen during preparation, we also imaged the membrane using the spectral line at 491 nm and a 525/50 band-pass filter.

Image sequence processing

We processed the fluorescence images using the following software packages: Andor iQ3 v3.1, ImageJ 1.52j, and custom written Matlab 2016a scripts. For better visualization, we additionally applied background correction and filtering of artifacts. In detail, these were carried out as follows: For the generation of the movies, each frame was first corrected for fluorescence bleaching (max. 20 % decay of the intensity for long movies) by normalizing to the mean intensity of the respective frame. Then, we generated two different modifications of the images: First, we averaged out all transient features (i.e., patterns) in the frames to obtain 'static background'-images which we shall call `Imstat`. Second, we smoothed out

the images, determined the average of all movie frames, and normalized the corresponding result with respect to its maximum. This way, we obtained an 'illumination correction' image `Imillum`. In the final step, each frame `Immovie` was corrected according to the rule `Imcorrected` = (`Immovie` - `Imstat`)/`Imillum`. On one hand, this ensures that irregularities in each image are suppressed, and on the other hand, the intensity amplitudes at the edges becomes comparable with the values at the center of the image.

References

[1] Alan M. Turing. The chemical basis of morphogenesis. *Philosophical Transactions of the Royal Society of London. Series B, Biological Sciences*, 237(641):37–72, 1952.

[2] Shigeru Kondo and Rihito Asai. A reaction–diffusion wave on the skin of the marine angelfish pomacanthus. *Nature*, 376(6543):765–768, 1995.

[3] Christopher A. Klausmeier. Regular and irregular patterns in semiarid vegetation. *Science*, 284(5421):1826–1828, 1999.

[4] J. B. A. Green and J. Sharpe. Positional information and reaction-diffusion: two big ideas in developmental biology combine. *Development*, 142(7):1203–1211, 2015.

[5] Jacob Halatek, Fridtjof Brauns, and Erwin Frey. Self-organization principles of intracellular pattern formation. *Philosophical Transactions of the Royal Society B: Biological Sciences*, 373(1747):20170107, 2018.

[6] M. C. Cross and P. C. Hohenberg. Pattern formation outside of equilibrium. *Reviews of Modern Physics*, 65(3):851–1112, 1993.

[7] N. Tompkins, N. Li, C. Girabawe, M. Heymann, G. B. Ermentrout, I. R. Epstein, and S. Fraden. Testing turing's theory of morphogenesis in chemical cells. *Proceedings of the National Academy of Sciences*, 111(12):4397–4402, 2014.

[8] Erwin Frey and Fridtjof Brauns. Self-organisation of protein patterns. *arXiv:2012.01797 [nlin, physics:physics]*, 2020. Comment: 134 pages, 41 figures.

[9] Andrew B. Goryachev and Marcin Leda. Many roads to symmetry breaking: molecular mechanisms and theoretical models of yeast cell polarity. *Molecular Biology of the Cell*, 28(3):370–380, 2017.

[10] Philipp Glock, Fridtjof Brauns, Jacob Halatek, Erwin Frey, and Petra Schwille. Design of biochemical pattern forming systems from minimal motifs. *eLife*, 8:e48646, 2019.

[11] Manon C. Wigbers, Tzer Han Tan, Fridtjof Brauns, Jinghui Liu, S. Zachary Swartz, Erwin Frey, and Nikta Fakhri. A hierarchy of protein patterns robustly decodes cell shape information. *Nature Physics*, pages 1–7, 2021.

[12] Uwe C. Täuber. *Critical dynamics: a field theory approach to equilibrium and non-equilibrium scaling behavior*. 2014.

[13] Robert Zwanzig. *Nonequilibrium statistical mechanics*. Oxford University Press, Oxford ; New York, 2001.

[14] J. Halatek and E. Frey. Rethinking pattern formation in reaction–diffusion systems. *Nature Physics*, 14(5):507, 2018.

[15] Fridtjof Brauns, Jacob Halatek, and Erwin Frey. Phase-space geometry of mass-conserving reaction-diffusion dynamics. *Physical Review X*, 10(4):041036, 2020.

[16] H. I. Adler, W. D. Fisher, A. Cohen, and A. A. Hardigree. Miniature escherichia coli cells deficient in dna. *Proceedings of the National Academy of Sciences*, 57(2):321–326, 1967.

[17] Piet A. J. de Boer, Robin E. Crossley, and Lawrence I. Rothfield. A division inhibitor and a topological specificity factor coded for by the minicell locus determine proper placement of the division septum in e. coli. *Cell*, 56(4):641–649, 1989.

[18] M. Loose, E. Fischer-Friedrich, J. Ries, K. Kruse, and P. Schwille. Spatial regulators for bacterial cell division self-organize into surface waves in vitro. *Science*, 320(5877):789–792, 2008.

[19] Erwin Frey, Jacob Halatek, Simon Kretschmer, and Petra Schwille. *Protein Pattern Formation*, pages 229–260. Springer International Publishing, Cham, 2018.

[20] Beatrice Ramm, Tamara Heermann, and Petra Schwille. The e. coli mincde system in the regulation of protein patterns and gradients. *Cellular and Molecular Life Sciences*, 76(21):4245–4273, 2019.

[21] V. Ivanov and K. Mizuuchi. Multiple modes of interconverting dynamic pattern formation by bacterial cell division proteins. *Proceedings of the National Academy of Sciences*, 107(18):8071–8078, 2010.

[22] Anthony G. Vecchiarelli, Min Li, Michiyo Mizuuchi, Ling Chin Hwang, Yeonee Seol, Keir C. Neuman, and Kiyoshi Mizuuchi. Membrane-bound minde complex acts as a toggle switch that drives min oscillation coupled to cytoplasmic depletion of mind. *Proceedings of the National Academy of Sciences*, 113(11):E1479–E1488, 2016.

[23] Jonas Denk, Simon Kretschmer, Jacob Halatek, Caroline Hartl, Petra Schwille, and Erwin Frey. Mine conformational switching confers robustness on self-organized min protein patterns. *Proceedings of the National Academy of Sciences*, 115(18):4553–4558, 2018.

[24] Thomas Litschel, Beatrice Ramm, Roel Maas, Michael Heymann, and Petra Schwille. Beating vesicles: Encapsulated protein oscillations cause dynamic membrane deformations. *Angewandte Chemie International Edition*, 57(50):16286–16290, 2018.

[25] Elisa Godino, Jonás Noguera López, David Foschepoth, Céline Cleij, Anne Doerr, Clara Ferrer Castellà, and Christophe Danelon. De novo synthesized min proteins drive oscillatory liposome deformation and regulate ftsa-ftsz cytoskeletal patterns. *Nature Communications*, 10(1):4969, 2019.

[26] Shunshi Kohyama, Natsuhiko Yoshinaga, Miho Yanagisawa, Kei Fujiwara, and Nobuhide Doi. Cell-sized confinement controls generation and stability of a protein wave for spatiotemporal regulation in cells. *eLife*, 8:e44591, 2019.

[27] Philipp Glock, Beatrice Ramm, Tamara Heermann, Simon Kretschmer, Jakob Schweizer, Jonas Mücksch, Gökberk Alagöz, and Petra Schwille. Stationary patterns in a two-protein reaction-diffusion system. *ACS Synthetic Biology*, 8(1):148–157, 2019.

[28] Fridtjof Brauns, Grzegorz Pawlik, Jacob Halatek, Jacob Kerssemakers, Erwin Frey, and Cees Dekker. Bulk-surface coupling identifies the mechanistic connection between min-protein patterns in vivo and in vitro. *Nature Communications*, 12(1), 2021.

[29] Anthony G. Vecchiarelli, Min Li, Michiyo Mizuuchi, and Kiyoshi Mizuuchi. Differential affinities of mind and mine to anionic phospholipid influence min patterning dynamicsin vitro. *Molecular Microbiology*, 93(3):453–463, 2014.

[30] Stuart Berg, Dominik Kutra, Thorben Kroeger, Christoph N. Straehle, Bernhard X. Kausler, Carsten Haubold, Martin Schiegg, Janez Ales, Thorsten Beier, Markus Rudy, Kemal Eren, Jaime I. Cervantes, Buote Xu, Fynn Beuttenmueller, Adrian Wolny, Chong Zhang, Ullrich Koethe, Fred A. Hamprecht, and Anna Kreshuk. ilastik: interactive machine learning for (bio)image analysis. *Nature Methods*, 16(12):1226–1232, 2019.

[31] Fridtjof Brauns, Jacob Halatek, and Erwin Frey. Diffusive coupling of two well-mixed compartments elucidates elementary principles of protein-based pattern formation. *Physical Review Research*, 3(1), 2021.

[32] Mariela D. Petkova, Gašper Tkačik, William Bialek, Eric F. Wieschaus, and Thomas Gregor. Optimal decoding of cellular identities in a genetic network. *Cell*, 176(4):844–855.e15, 2019.

[33] Fridtjof Brauns, Henrik Weyer, Jacob Halatek, Junghoon Yoon, and Erwin Frey. Wavelength selection by interrupted coarsening in reaction-diffusion systems. *Physical Review Letters*, 126(10), 2021.

[34] D. M. Winterbottom, S. M. Cox, and P. C. Matthews. Pattern formation in a model of a vibrated granular layer. *SIAM Journal on Applied Dynamical Systems*, 7(1):63–78, 2008.

[35] Igor S. Aranson and Lev S. Tsimring. Patterns and collective behavior in granular media: Theoretical concepts. *Reviews of Modern Physics*, 78(2):641–692, 2006.

[36] M. C. Marchetti, J. F. Joanny, S. Ramaswamy, T. B. Liverpool, J. Prost, Madan Rao, and R. Aditi Simha. Hydrodynamics of soft active matter. *Reviews of Modern Physics*, 85(3):1143–1189, 2013.

[37] Markus Bär, Robert Großmann, Sebastian Heidenreich, and Fernando Peruani. Self-propelled rods: Insights and perspectives for active matter. *Annual Review of Condensed Matter Physics*, 11(1):441–466, 2020.

[38] Jonas Denk and Erwin Frey. Pattern-induced local symmetry breaking in active-matter systems. *Proceedings of the National Academy of Sciences*, 117(50):31623–31630, 2020.

[39] Olivier Dauchot and Hartmut Löwen. Chemical physics of active matter. *The Journal of Chemical Physics*, 151(11), 2019.

[40] Robert Großmann, Igor S. Aranson, and Fernando Peruani. A particle-field approach bridges phase separation and collective motion in active matter. *Nature Communications*, 11(1), 2020.

[41] Andrew L. Krause, Václav Klika, Thomas E. Woolley, and Eamonn A. Gaffney. From one pattern into another: analysis of turing patterns in heterogeneous domains via wkbj. *Journal of The Royal Society Interface*, 17(162), 2020.

[42] Karen Page, Philip K. Maini, and Nicholas A. M. Monk. Pattern formation in spatially heterogeneous turing reaction–diffusion models. *Physica D: Nonlinear Phenomena*, 181(1-2):80–101, 2003.

[43] D. Benson, J. Sherratt, and P. Maini. Diffusion driven instability in an inhomogeneous domain. *Bulletin of Mathematical Biology*, 55(2):365–384, 1993.

[44] Rohit Supekar, Boya Song, Alasdair Hastewell, Alexander Mietke, and Jörn Dunkel. Learning hydrodynamic equations for active matter from particle simulations and experiments. *arXiv:2101.06568 [cond-mat, physics:physics]*, 2021.

[45] Teeratorn Kadeethum, Thomas M. Jørgensen, and Hamidreza M. Nick. Physics-informed neural networks for solving nonlinear diffusivity and biot's equations. *Plos One*, 15(5), 2020.

[46] Maziar Raissi, Paris Perdikaris, and George Em Karniadakis. Physics informed deep learning (part i): Data-driven solutions of nonlinear partial differential equations. *arXiv:1711.10561 [cs, math, stat]*, 2017.

[47] K. C. Huang, Y. Meir, and N. S. Wingreen. Dynamic structures in escherichia coli: Spontaneous formation of mine rings and mind polar zones. *Proceedings of the National Academy of Sciences*, 100(22):12724–12728, 2003.

[48] Jacob Halatek and Erwin Frey. Highly canalized mind transfer and mine sequestration explain the origin of robust mincde-protein dynamics. *Cell Reports*, 1(6):741–752, 2012.

[49] Martin Loose, Karsten Kruse, and Petra Schwille. Protein self-organization: Lessons from the min system. *Annual Review of Biophysics*, 40(1):315–336, 2011.

[50] G. Meacci, J. Ries, E. Fischer-Friedrich, N. Kahya, P. Schwille, and K. Kruse. Mobility of min-proteins in ¡i¿escherichia coli¡/i¿ measured by fluorescence correlation spectroscopy. *Physical Biology*, 3(4):255–263, 2006.

[51] Yaron Caspi and Cees Dekker. Mapping out min protein patterns in fully confined fluidic chambers. *eLife*, 5, 2016.